INTERNATIONAL JOURNAL FOR NUMERICAL METHODS IN FLUIDS
Int. J. Numer. Meth. Fluids 2004; **46**:637–661 (DOI: 10.1002/fld.771)

Transient free-surface flow of a viscoelastic fluid in a narrow channel

Roger E. Khayat*,† and Runling Pan

Department of Mechanical and Materials Engineering, The University of Western Ontario, London, Ont., Canada N6A 5B9

SUMMARY

The interplay between inertia and elasticity is examined for transient free-surface flow inside a narrow channel. The lubrication theory is extended for the flow of viscoelastic fluids of the Oldroyd-B type (consisting of a Newtonian solvent and a polymeric solute). While the general formulation accounts for non-linearities stemming from inertia effects in the momentum conservation equation, and the upper-convected terms in the constitutive equation, only the front movement contributes to non-linear coupling for a flow inside a straight channel. In this case, it is possible to implement a spectral representation in the depthwise direction for the velocity and stress. The evolution of the flow field is obtained locally, but the front movement is captured only in the mean sense. The influence of inertia, elasticity and viscosity ratio is examined for pressure-induced flow. The front appears to progress monotonically with time. However, the velocity and stress exhibit typically a strong overshoot upon inception, accompanied by a plug-flow behaviour in the channel core. The flow intensity eventually diminishes with time, tending asymptotically to Poiseuille conditions. For highly elastic liquids the front movement becomes oscillatory, experiencing strong deceleration periodically. A multiple-scale solution is obtained for fluids with no inertia and small elasticity. Comparison with the exact (numerical) solution indicates a wide range of validity for the analytical result. Copyright © 2004 John Wiley & Sons, Ltd.

KEY WORDS: thin-cavity flow; free surface; viscoelastic; multiple scale

1. INTRODUCTION

The flow of a thin film inside cavities is of relevance to lubrication, injection molding and die casting problems. Despite the wide body of studies in the literature, the modelling and simulation of film flow remain challenging under conditions where non-linear effects are important. Non-linearities may stem from material behaviour such as inertia or non-Newtonian (shear-thinning and viscoelastic) effects, or from geometry such as in the presence of a

*Correspondence to: R. E. Khayat, Department of Mechanical and Materials Engineering, The University of Western Ontario, London, Ont., Canada N6A 5B9.
†E-mail: rkhayat@eng.uwo.ca

Contract/grant sponsor: Natural Sciences and Engineering Research Council of Canada

Published online 6 September 2004

Received 21 July 2003
Revised 2 April 2004

moving free surface or interface. The interplay between material and geometric non-linearities is the focus of the present study, which is examined during the development of early transient free-surface flow of a viscoelastic fluid inside a narrow channel under the action of a driving pressure.

Regarding the simulation of free surface flow of viscoelastic fluids, one is faced, on the one hand, with the incapacity of conventional domain methods to deal with the issue of adaptive meshing for moving-boundary flows [1], and, on the other hand, with the failure of integral methods to deal with non-linearities [2]. Due to limited computational resources, the three-dimensional flow problem has customarily been simplified to a two-dimensional problem, based on the observation of Hele-Shaw [3]. The method is closely related to the lubrication or shallow-water theory for Newtonian flow. In this approach, the cavity is assumed to be thin, and out of plane flows are neglected. Richardson [4] was the first to propose this method for molding flow. He examined Newtonian, isothermal flow inside cavities of simple geometry. Three decades later, the lubrication assumption remains the basis for the simulation of free surface flow of thin films [5–7]. Whilst all of the related mathematical models used in the literature stem from the common (and justifiable) assumption of constant pressure distribution in the depthwise direction, further restrictive assumptions, which are usually introduced without quantitative justification, result in the creation of mathematical formulations with different capabilities. In particular, (i) formulations in which the depthwise distribution of the streamwise velocity component is variable and allows the study of return flows [8], and (ii) formulations in which only the mean streamwise velocity is considered [9].

Although the thin-film formulation reduces the pressure to its hydrostatic part, thus eliminating the momentum equation in the depthwise direction from the problem, the dimension of the problem remains the same as the original equations. The dimension of the problem is reduced by imposing an approximate (usually parabolic) flow profile in the depthwise direction. However, such a profile is not valid under all flow conditions, such as in the presence of end effects, for a turbulent flow or at high Reynolds number [10–12], or, very likely, when other non-linear effects such as shear-thinning or viscoelastic effects are included. A more rigorous solution procedure to the lubrication equations becomes almost as difficult to achieve as to the original Navier–Stokes equations. Recently, Khayat proposed an accurate low-dimensional spectral approach to the flow of a thin coating film over two-dimensional substrates of arbitrary shape [13]. The study, however, is limited to Newtonian fluids.

The present paper addresses the solution of a large class of free-surface flows with close relevance to materials processing. Since both inertia and viscoelastic effects are included, the work is equally relevant to die casting and injection molding. These problems are typically concerned with the filling stage inside a thin cavity and die flow. The lubrication assumption is adopted to derive the resultant equations for an Oldroyd-B fluid. A spectral representation of the velocity and stress is assumed. The influence of inertia and elasticity on the evolution of the front, the shear and normal forces for a flow in a narrow channel is examined in some detail. The solution for an inertialess (purely elastic) fluid is also obtained using the method of multiple scales.

2. PROBLEM FORMULATION AND SOLUTION PROCEDURE

In this section, the generalized lubrication equations and boundary conditions are derived for narrow channel flow of a viscoelastic fluid. The solution procedure is then outlined.

2.1. General lubrication equations for an Oldroyd-B fluid

Consider an incompressible viscoelastic fluid of density ρ, relaxation time λ, viscosity η, and surface-tension coefficient γ. In this study, only fluids that can be reasonably represented by a single relaxation time and constant viscosity are considered. Regardless of the nature of the fluid, the continuity and momentum balance equations must hold. If (x_1, x_2) denotes the two-dimensional system of coordinates, then the conservation equations for an incompressible fluid can be concisely written as:

$$u_{j,j} = 0, \quad \rho(u_{i,T} + u_j u_{i,j}) = \sigma_{ji,j} \tag{1}$$

where $i,\ j = 1, 2$. Here the summation convention is assumed, and a comma denotes partial differentiation. T is the time, and σ_{ij} are the components of the total stress tensor that is assumed to be symmetric. In the present work, the deviatoric part of the stress tensor is taken to be composed of a Newtonian component, corresponding to the solvent, and a polymeric component, τ_{ij}, corresponding to the solute. Thus,

$$\sigma_{ij} = -\Pi\delta_{ij} + \eta_s(u_{i,j} + u_{j,i}) + \tau_{ij} \tag{2}$$

where Π is the hydrostatic pressure, and η_s is the viscosity of the (Newtonian) solvent. The constitutive equation for τ_{ij} corresponds to an Oldroyd-B fluid, which can be written as [14]:

$$\lambda(\tau_{ij,T} + u_k\tau_{ij,k} - \tau_{ik}u_{j,k} - \tau_{jk}u_{i,k}) + \tau_{ik} = \eta_p(u_{i,j} + u_{j,i}) \tag{3}$$

where η_p is the viscosity of the polymeric solute. Thus, the viscosity of the solution is given by $\eta = \eta_s + \eta_p$. In the limit $\eta_s \to 0$, system (1)–(3) reduces to that corresponding to a Maxwell fluid. On the other hand, in the limit $\eta_s \to \infty$, the equations for a Newtonian fluid are recovered. This is also equivalent to setting the relaxation time, λ_1, equal to the retardation time, λ_2, of the fluid [14]. Note that $\lambda_1 = \lambda;\ \lambda_2 = \lambda(\eta_s/\eta_s + \eta_p)$, so that $\lambda_2 \leqslant \lambda_1$.

The equations above are now formulated in the narrow-gap limit. It is convenient to cast Equations (1) and (3) in terms of dimensionless variables. Typically, in thin-cavity flow, there are two characteristic lengths, L, in the streamwise direction, x_1, and a height, H, representing the thickness of the cavity in the depthwise direction, x_2. Figure 1 illustrates schematically the general flow and notations used. The dimensionless variables may be introduced as follows:

$$\begin{gathered} x = \frac{x_1}{L}, \quad z = \frac{x_2}{\varepsilon L}, \quad t = \frac{L}{V}T \\ u_x = \frac{u_1}{V}, \quad u_z = \frac{u_2}{V\varepsilon}, \quad p = \frac{\varepsilon^2 L}{\eta V}\Pi \\ \tau_{xx} = \frac{\varepsilon^2 L}{\eta V}\tau_{11}, \quad \tau_{zz} = \frac{L}{\eta V}\tau_{22}, \quad \tau_{xz} = \frac{\varepsilon L}{\eta V}\tau_{12} \end{gathered} \tag{4}$$

where $\varepsilon = H/L$ is the aspect ratio, and V is a typical (reference) velocity. In addition to ε, there are three important dimensionless groups, namely, the Reynolds number, *Re*, the Deborah number, *De*, and the solvent-to-solute viscosity ratio, *Rv*. These parameters are explicitly written:

$$Re = \frac{\rho VL}{\eta}, \quad De = \frac{\lambda V}{L}, \quad Rv = \frac{\eta_s}{\eta_p} \tag{5}$$

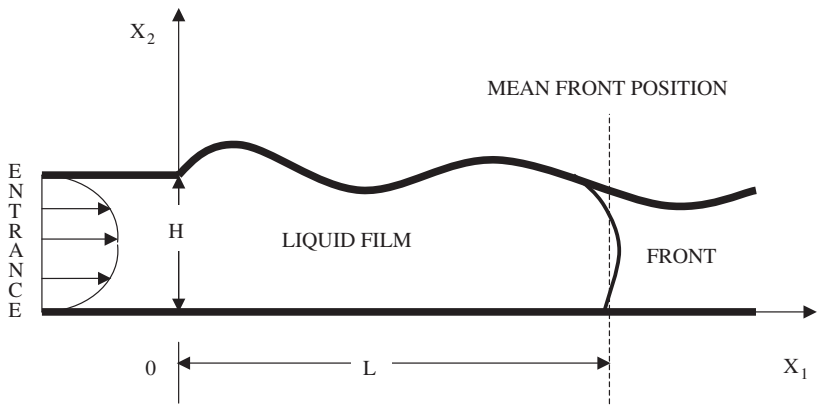

Figure 1. Schematic view and notations used for typical moving-boundary flow inside a thin channel.

In dimensionless form, and if terms of $O(\varepsilon^2)$ and higher are excluded, then Equation (1) reduce to:

$$u_{x,x} + u_{z,z} = 0 \tag{6}$$

$$\varepsilon^2 Re(u_{x,t} + u_x u_{x,x} + u_z u_{x,z}) = -p_{,x} + aRv u_{x,zz} + \tau_{xx,x} + \tau_{xz,z}, \quad p_{,z} = 0 \tag{7}$$

The term $\varepsilon^2 Re$ is not necessarily negligible since Re may be large enough for the term to be of order one. In this work, inertia effects will be accounted for to cover a wide range of applications. The resultant stress equations are given by:

$$De(\tau_{xz,t} + u_x \tau_{xz,x} + u_z \tau_{xz,z} - \tau_{xx} u_{z,x} - \tau_{zz} u_{x,z}) + \tau_{xz} = a u_{x,z} \tag{8a}$$

$$De(\tau_{xx,t} + u_x \tau_{xx,x} + u_z \tau_{xx,z} - 2\tau_{xx} u_{x,x} - 2\tau_{xz} u_{x,z}) + \tau_{xx} = 0 \tag{8b}$$

$$De(\tau_{zz,t} + u_x \tau_{zz,x} + u_z \tau_{zz,z} - 2\tau_{zx} u_{z,x} - 2\tau_{zz} u_{z,z}) + \tau_{zz} = a u_{z,z} \tag{8c}$$

where $a = 1/(Rv + 1)$. The scaling with respect to ε^2 for the pressure and normal stress, and ε for the shear stress, results from the balance of the linear and non-linear terms in the momentum and constitutive equations. The Navier–Stokes equations are recovered from Equations (6)–(8) by taking the limit $Rv \to \infty$, which corresponds to taking an infinite viscosity for the solvent. In this limit, the linear terms in velocity on the right-hand side of Equations (8) vanish, and the polymeric stress equations admit zero-stress solutions. Since the product $aRv = 1$ when Rv is infinite, the momentum equation reduces to the Newtonian form.

2.2. Boundary conditions

Stick boundary conditions are applied at the bottom and upper channel surfaces. The flow is assumed to be driven by the action of an imposed pressure at the channel entrance $x = 0$. The pressure is maintained fixed at all time. This corresponds typically to the inlet condition in injection molding where the pressure rather than the flow rate may be fixed at the source of

fluid. If the front profile is given by $x = f(z,t)$, then the kinematic boundary condition may be written as:

$$u_x(x = f, z, t) = f_{,t}(z,t) + u_z(z,t) f_{,z}(z,t) \tag{9}$$

An important expression for the velocity at the channel entrance is obtained upon integrating Equation (6) over the range $x \in [0, f]$ and using relation (9), namely,

$$u_x(x = 0, z, t) = f_{,t}(z,t) + \frac{\partial}{\partial z} \int_0^{f(z,t)} u_z(x, z, t)\, \mathrm{d}x \tag{10}$$

In thin-film or lubrication theory, the depthwise velocity is one order of magnitude smaller than the streamwise component, as (4) indicates, and is often neglected. In this case, Equation (10) suggests that the velocity at the channel entrance is equal to the rate of front movement. Note that the integration of Equation (10) over the channel depth leads to another important relation between the mean velocity at $x = 0$ and the rate of change in mean front position (see below).

The imposition of a suitable dynamic condition is not obvious for thin-film flow. Let $\mathbf{n}(z,t)$ and $\mathbf{s}(z,t)$ be the normal and tangent unit vectors at the front. The dynamic condition at $x = f(z,t)$, becomes

$$\begin{aligned}(2aRv\varepsilon^2 u_{x,x} + \tau_{xx}) s_x n_x + \varepsilon^2 (2aRv u_{z,z} + \tau_{zz}) s_z n_z \\ + \varepsilon [aRv(u_{x,z} + \varepsilon^2 u_{z,x}) + \tau_{xz}](s_x n_z + s_z n_x) = 0\end{aligned} \tag{11a}$$

along the tangential direction, and

$$\begin{aligned}-p + (2aRv\varepsilon^2 u_{x,x} + \tau_{xx}) n_x^2 + \varepsilon^2 (2aRv u_{z,z} + \tau_{zz}) n_z^2 \\ + 2\varepsilon [aRv(u_{x,z} + \varepsilon^2 u_{z,x}) + \tau_{xz}] n_x n_z = \frac{\varepsilon}{Ca}(\varepsilon n_{x,x} + n_{z,z})\end{aligned} \tag{11b}$$

along the normal direction. Here $Ca = \eta V/\gamma$ is the capillary number. It should be emphasized at this stage that an assessment of the order of magnitude for each term in Equations (11) can be made only when the components of the unit normal vector (n_x, n_z) and unit tangent (s_x, s_z) to the front are given. These components are expressed as

$$n_x(z,t) = -s_z(z,t) = \frac{\varepsilon}{\sqrt{\varepsilon^2 + f_{,z}^2}}, \quad n_z(z,t) = s_x(z,t) = -\frac{f_{,z}}{\sqrt{\varepsilon^2 + f_{,z}^2}} \tag{12}$$

where it is assumed that normal and tangent vectors can be defined everywhere along the front. Conditions (11) reduce considerably when only leading terms are retained. Upon substituting expressions (12), Equation (11a) is found to be identically satisfied. Equation (11b) reduces to an expression relating the pressure to surface tension effect, namely

$$p(x = f, z, t) = \frac{\varepsilon^3}{Ca} f_{,z} f_{,zz} \tag{13}$$

The resulting dynamic condition is the same as for Newtonian flow. However, for viscoelastic fluids, surface tension is typically small and Ca is of order 1 or higher [15]. In this case, it is safe to neglect surface tension effect, leading to the vanishing of the pressure at the front (see also below).

2.3. The reduced problem

In this study, the flow is assumed by an imposed constant pressure gradient at the channel entrance. In accord with the lubrication assumption, the pressure at $x=0$ is assumed to be uniform along the depth. The entrance pressure, $P(t)$, is maintained fixed at all time. This corresponds typically to the inlet condition in injection molding where the pressure rather than the flow rate may be fixed at the source of fluid. Since the aim of the present work is to explore the interplay of inertia and elasticity, the geometrical aspects become less significant. Thus, the channel will be assumed to be straight. In this case, the pressure decreases linearly from $P(t)$ at $x=0$ to zero at the front, $x=X$. Consequently, given the depthwise uniformity of the pressure and pressure gradient, the evolution of the front can only be captured in the average sense, again in accord with the lubrication formulation. Thus, the average front position is defined by

$$X(t)=\int_0^1 f(z,t)\,\mathrm{d}z \tag{14}$$

The domain of computation is then $(x,z)\in[0,1]\times[0,X(t)]$. In this case, L corresponds to the initial (average) length.

The relevant equations for velocity and stress are deduced from Equations (6)–(8), namely,

$$\delta u_{x,t}=aRvu_{x,zz}+\tau_{xz,z}+\frac{P}{X} \tag{15}$$

$$De\tau_{xz,t}+\tau_{xz}=au_{x,z} \tag{16}$$

$$De(\tau_{xx,t}-2\tau_{xz}u_{x,z})+\tau_{xx}=0 \tag{17}$$

where $\delta=\varepsilon^2 Re$. In this case, τ_{zz} is identically zero, and τ_{xx} becomes the normal stress difference. Again, the Newtonian form of the above equations is recovered by taking the limit $Rv\to\infty$. In this case, one recovers the lubrication equation that is identical to the channel flow equation with variable pressure gradient. In this case, the velocity and shear stress components are decoupled from the normal stress. Although Equations (15) and (16) are linear in velocity and stress, the problem is inherently non-linear because of the coupling with front movement. The no-slip condition leads to:

$$u_x(z=0,t)=u_x(z=1,t)=0 \tag{18}$$

The kinematic boundary condition also applies at the front, which reads:

$$\dot{X}(t)=U(t)\equiv\int_0^1 u_x(z,t)\,\mathrm{d}z \tag{19}$$

where a dot denotes total differentiation with respect to t, and $U(t)$ is of course the mean velocity at the front. The Newtonian and shear-thinning problem equivalent to (12)–(15) has

been addressed before in the literature, particularly in relation to injection molding. For more details on this problem in channel and radial flows, the reader is referred to the monographs by Middleman [16] and Watson [17], and the references therein.

As to the initial conditions, it will be assumed that the fluid is initially at rest upon inception. It will be assumed that the polymeric contribution to stress is negligible upon inception. Thus,

$$u_x(z,t=0)=\tau_{xz}(z,t=0)=\tau_{xx}(z,t=0)=0 \tag{20}$$

This is a realistic assumption since elastic effects are not expected to be significant initially, given the small shear and elongational flows. Additionally,

$$X(t=0)=1 \tag{21}$$

It is helpful at this stage to introduce the total shear stress as $s(z,t)=aRvu_{x,z}(z,t)+\tau_{xz}(z,t)$. Also let the stresses at the wall $z=0$ be defined by $S(t)=s(z=0,t)$, $T(t)=\tau_{xz}(z=0,t)$ and $N(t)=\tau_{xx}(z=0,t)$. The solution to the initial-boundary-value problem above is discussed next.

2.4. Solution procedure

Since the normal stress is decoupled from the velocity and shear stress, a solution to Equations (15) and (16) is sought in the form of Fourier series representation for the velocity and shear stress, which satisfy conditions (18):

$$u_x(z,t)=\sum_{n=1}^{M} u_x^n(t)\sin[(2n-1)\pi z], \quad \tau_{xz}(z,t)=\sum_{n=1}^{M}\tau_{xz}^n(t)\cos[(2n-1)\pi z] \tag{22}$$

where M is the number of modes. The time-dependent coefficients, u_x^n and τ_{xz}^n are clearly governed by the equations:

$$\delta\dot{u}_x^n=-(2n-1)^2\pi^2 aRvu_x^n+(2n-1)\pi\tau_{xz}^n+\frac{4P}{X} \tag{23}$$

$$De\dot{\tau}_{xz}^n=-\tau_{xz}^n+(2n-1)\pi a u_x^n \tag{24}$$

which are obtained upon substituting expressions (22) into and projecting Equations (15) and (16) onto each mode. In accord with (20), the coefficients must be zero at $t=0$. Note that a dot denotes differentiation with respect to time. In this case, Equation (19) reduces to

$$\dot{X}(t)=\frac{2}{\pi}\sum_{n=1}^{M}\frac{u_x^n(t)}{2n-1} \tag{25}$$

For a Newtonian fluid, the problem can be reduced to an integro-differential equation in X (see below). It is observed that, even in this case, the direct solution of the system of ODEs (23)–(25) is numerically much easier than the numerical solution of the integro-differential equation, and thus the former route is the one that is taken in this study.

The expression for the normal stress follows from solutions (22) and Equation (21). Thus, let

$$\tau_{xx}(z,t)=\sum_{m=1}^{M}\sum_{n=1}^{M}\tau_{xx}^{mn}(t)\cos[(2m-1)\pi z]\cos[(2n-1)\pi z] \tag{26}$$

where the coefficients $\tau_{xx}^{mn}(t)$ are governed by

$$De\dot{\tau}_{xx}^{mn} = -\tau_{xx}^{mn} + 2De(2m-1)\pi a u_x^m \tau_{xz}^n \tag{27}$$

Equations (23)–(25) and (27) constitute a set of $3M+1$ degrees, which are solved subject to

$$u_x^n(t=0) = \tau_{xz}^n(t=0) = 0, \quad X(t=0) = 1 \tag{28}$$

The time-dependent coefficients and $X(t)$ are obtained using a sixth-order Runge–Kutta scheme (IMSL-DIVPRK). The accuracy of the solution was checked using Gear's predictor-corrector method (IMSL-DIVPAG). The results from both methods are essentially identical when the same time increment is used. In both methods, a tolerance of less than 10^{-6} is used. That is, the norm of the local error is controlled such that the global error is less than the tolerance imposed. Additional accuracy assessment is reported below.

3. LIMIT FLOWS AND PRELIMINARY RESULTS

In anticipation of the numerical results for arbitrary values of the parameters, it is useful to examine limit cases. These include the flows of Newtonian fluids, purely elastic (inertialess) fluids, and asymptotic flow behaviour at large time for any fluid.

3.1. Newtonian flow

The Newtonian limit corresponds to a solution with only the solvent ($\eta_p = 0$). This limit is thus recovered by setting $Rv \to \infty$. In this case the product $aRv = 1$, and $a = 0$. These limit values lead to the vanishing of the polymeric shear and normal stresses. For Newtonian flow, an integrating factor can be found, and the problem (23)–(24) is recast as a non-linear integro-differential equation for $X(t)$ if $P(t)$ is prescribed, or an integral equation for $P(t)$ if the flow rate is imposed. Thus, the problem reduces to

$$\dot{X}(t) = \frac{8}{\delta} \sum_{n=1}^{M} \frac{1}{a_n} \int_0^t \frac{P(\tau)}{X(\tau)} \mathrm{e}^{-a_n/\delta(t-\tau)}\, \mathrm{d}\tau \tag{29}$$

where $a_n = [(2n-1)\pi]^2$. In the absence of inertia ($\delta \to 0$), the solution is easily obtained as

$$X(t) = \sqrt{\frac{Pt}{6} + 1}, \quad U(t) = \frac{P}{12\sqrt{Pt/6+1}} \tag{30}$$

Note that the initial velocity is not zero in general.

3.2. Purely elastic flow

In the absence of inertia, elastic and viscous effects are the only balancing forces. This is an important limit since most viscoelastic fluids exhibit very little inertia effect, at least under normal flow conditions. If $\delta = 0$, Equation (15) is readily integrated, and the velocity and shear stresses may be written as:

$$u_x(z,t) = 6U(t)(z-1)z, \quad \tau_{xz}(z,t) = T(t)(1-2z), \quad \tau_{xx}(z,t) = N(t)(1-2z)^2 \tag{31}$$

which, after some algebraic manipulation, give the following equation for X and corresponding initial conditions:

$$12aRvDeX^2\ddot{X} + (12X^2 + DeP)\dot{X} - (De\dot{P} + P)X = 0 \tag{32a}$$

$$X(t=0) = 1, \quad \dot{X}(t=0) = \frac{P(0)}{12aRv} \tag{32b}$$

Note that the initial velocity is no longer generally zero, and depends only on the viscosity ratio. Similarly, the total shear stress experiences an initial jump equal to $P(0)/2$, which is independent from flow parameters. It is inferred from (32b) that the initial front velocity behaves like $1/Rv$ for small Rv, and becomes singular in the limit of a Maxwell fluid. This is an important feature that, as will be seen below, can have a drastic consequence on the response of fluids with low solvent-to-solute viscosity ratio. Equation and conditions (32) indicate that the front advancement depends only on the solvent-to-solution viscosity ratio, aRv. The normal stress at the wall is given by

$$N(t) = 2\int_0^t \dot{X}(t') \int_0^{t'} \dot{X}(t'')\mathrm{e}^{(t''-t')/De}\,\mathrm{d}t''\,\mathrm{d}t' \tag{33}$$

For a Maxwell fluid ($Rv = 0$), Equation (32) becomes singular, and the fluid experiences an initial jump in the velocity. If, further, the driving pressure is constant, $P(t) = 1$, the following relation is obtained:

$$De \ln X + 6X^2 = t + 6 \tag{34}$$

It is interesting to note in this case that the behaviours at small and large time are similar. In fact, for small t ($t \ll 6$), X becomes close to 1 and $X(t) \sim \sqrt{t/6 + 1}$, and for large t ($t \gg 6$), the quadratic term is also dominant with $X(t) \sim \sqrt{t/6}$.

More generally, problem (32) must be solved numerically. However, for small Rv and/or De, a multiple-scale solution is possible. As was mentioned earlier, the limit flow of a purely elastic fluid or inertialess fluid is singular near inception, and thus exhibit a behaviour of the 'boundary-layer' type. Note that the initial acceleration is given by $\ddot{X}(0) = 1/12aRvDe$. Consider then the solution of problem (32) for small Deborah number. Given the singularity at $De = 0$, a regular perturbation expansion in De is inadequate. Here the method of multiple scales is used to obtain the solution as $De \to 0$. It is suspected, through simple inspection of the governing equation, and as it is indeed confirmed from the numerical solution below, that the flow exhibits a 'boundary-layer' of thickness De near $t = 0$, and varies slowly in the range $De \ll t$ ($De \to 0^+$). Thus, there are two natural scales for this problem, a short scale t', which describes the inner solution in the boundary layer, and a long scale $t = De\,t'$, which describes the outer solution. Note that Equations (32) is written in terms of the long scale. An outline for the solution for small De and $P(t) = 1$ is given in Appendix A, with the result

$$X(t) = \sqrt{\frac{t}{6} + d_1} + d_2\mathrm{e}^{-t/aRvDe} + O(De), \quad De \to 0^+ \tag{35}$$

where d_1 and d_2 are constants given in Appendix A. It is interesting to observe from (A8) and (35) that $1/aRvDe$ is a similarity parameter in the approximate solution, whereas it is not in the original problem (32). This similarity has an important implication: One can expect

the approximation to hold not only for small De, but for small $aRvDe$ as well. Only the Newtonian limit can be recovered from Equation (35) by setting $De=0$ and $aRv=1$. The limit of a Maxwellian flow cannot be recovered from Equation (35); by simply setting $Rv\to 0$, one recovers again the Newtonian limit. This apparent paradox is resolved once one observes that the Maxwellian limit presents a singularity near $Rv=0$. This flow is recovered only if a singular perturbation expansion, similar to the one near $De=0$, is applied near $Rv=0$.

3.3. Long-term flow behaviour

Finally, consider the asymptotic behaviour of the flow field and stress when t is large for any δ, De and Rv values. In this case, problem (15)–(19) admits a quasi-steady-state solution upon setting the time derivatives equal to zero. It is not difficult to see that the asymptotic form of the velocity is the same as Poiseuille flow, so that

$$u_x(z,t)=\frac{P}{12X}z(1-z),\quad \tau_{xz}(z,t)=\frac{aP}{12X}(1-2z),\quad \tau_{xx}(z,t)=\frac{aDeP^2}{72X^2}(1-z)^2 \tag{36}$$

which upon substitution into (17), leads to the following equation for X:

$$\dot{X}=\frac{P}{12X} \tag{37}$$

Thus, the front moves at a velocity that decreases with front position. More specifically, the asymptotic forms of the front position, velocity and polymeric stresses are given by

$$X\sim\sqrt{\frac{Pt}{6}},\quad U\sim\sqrt{\frac{P}{2t}},\quad T\sim a\sqrt{\frac{P}{2t}},\quad N\sim\frac{aDeP}{12t} \tag{38}$$

It is interesting to note from (36) and (38) that, while the velocity and shear stress decay like $1/\sqrt{t}$, the normal stress decays like $1/t$, at large t. It is also important to note that the asymptotic behaviour of the front position and velocity is independent of δ, Rv and De, whereas that of the shear stress depends only Rv, and the normal stress depends on both De and Rv. This universal asymptotic behaviour is further confirmed by comparing expressions (30), (35) and the asymptotic solution of Equation (38).

4. DISCUSSION AND RESULTS

In this section, the influence of inertia, elasticity, and viscosity ratio is examined for a flow induced by a driving pressure gradient at the channel entrance. In particular, the evolution of the front position, front velocity, and stress buildup is explored in some detail. A multiple-scale solution is also obtained in the limit of inertialess fluid, for small Deborah number. Numerical accuracy and convergence are also assessed.

4.1. Influence of inertia

The effect of inertia is examined by varying δ and keeping the other parameters fixed. The solvent-to-polymeric viscosity ratio and the Deborah number are fixed at $Rv=1$ and $De=10$, respectively, and $\delta\in[0,200]$. The case of an inertialess fluid ($\delta=0$) is included for reference. The simulation is carried out over a period of 100 time units; most of the interesting transient

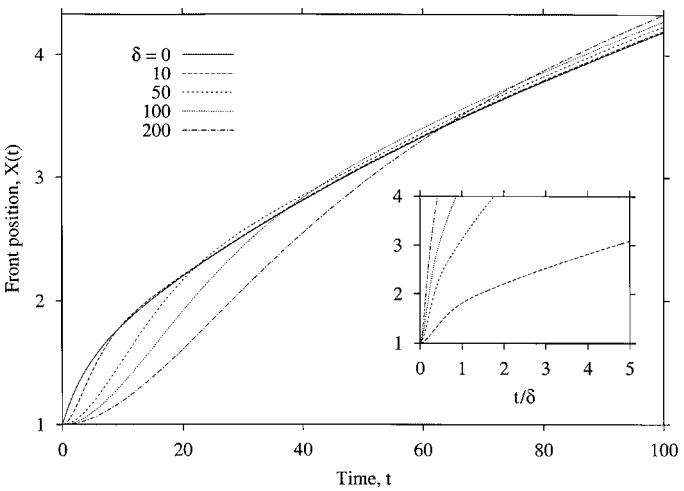

Figure 2. Influence of inertia on the evolution of the front position for a flow with $De = 10$, $Rv = 1$ and $\delta \in [0, 200]$. Inset shows X against t/δ.

behaviour occurs during this period. The evolution of the mean position of the front, $X(t)$, is shown in Figure 2, which displays a sharp increase in the early stages when δ is small, although the initial slope is zero except for $\delta = 0$. The front position is affected significantly by inertia, especially in the initial stages. For an inertialess fluid, the first of conditions (18) cannot be accommodated, and the fluid experiences instantaneous motion upon inception. In this case, the front continuously decelerates with time, but eventually moves at constant velocity. As δ increases (from zero), the fluid remains at rest initially, accelerating, and decelerating eventually similarly to inertialess flow. Figure 2 shows that for large t, inertia has essentially no effect, an observation that is anticipated from expressions (35). Finally, note that the time scale used for t in the figure is not most appropriate for quantitative assessment. However, this scale allows amplification of early behaviour. A more relevant (dimensionless) time is t/δ, which leads to the behaviour shown in the inset, reflecting the faster movement of the front as δ increases. Inertia is observed to be less influential for large δ.

The behaviour above is confirmed from Figure 3, where the evolution of the front velocity, $U(t)$, is depicted. For $\delta = 0$, the U exhibits an initial jump, which from Equation (29b), is equal to $\frac{1}{6}$. Thus, in the absence of inertia, the fluid velocity adjusts instantly to the driving pressure. In this case, and as illustrated in Figure 3, the front velocity decreases monotonically with time. For $\delta \neq 0$, $U(t)$ increases rapidly initially, exhibiting growth typical of 'boundary-layer' structure. $U(t)$ reaches a maximum, $U_{\max}$, then decreases monotonically with time, eventually reaching the same asymptotic (at large t) behaviour as for a fluid without inertia, as suggested by (35). The maximum decreases rapidly, becoming simultaneously weaker, as δ increases. The inset in Figure 3 shows the dependence of $U_{\max}$ and the time at which the maximum occurs, $t_{\max}$, on δ. It is found that both $U_{\max}$ and $t_{\max}/\delta$ behave like $\delta^{-1.8}$ and $\sqrt[3]{\delta}$, respectively. This behaviour appears to be consistent for other values of De and Rv, at least over practical ranges of these parameters (see below). A closer quantitative understanding

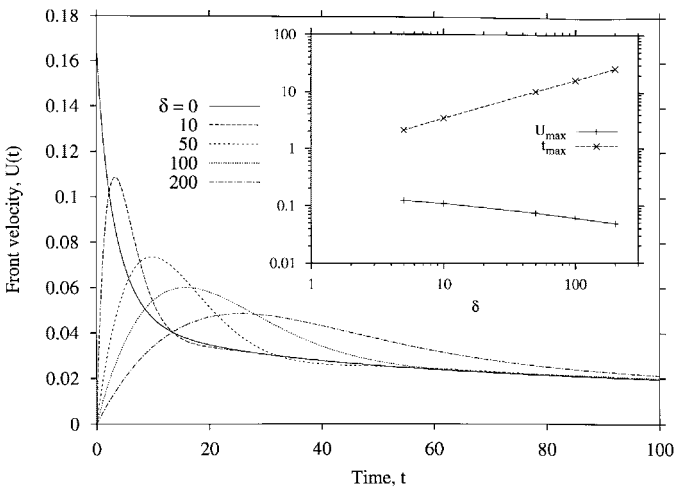

Figure 3. Influence of inertia on the evolution of the velocity, $U(t)$, of the front for a flow with $De = 10$, $Rv = 1$ and $\delta \in [0, 200]$. Inset shows the dependence of the velocity maximum, $U_{\max}$, and correspondence time, $t_{\max}$, on δ.

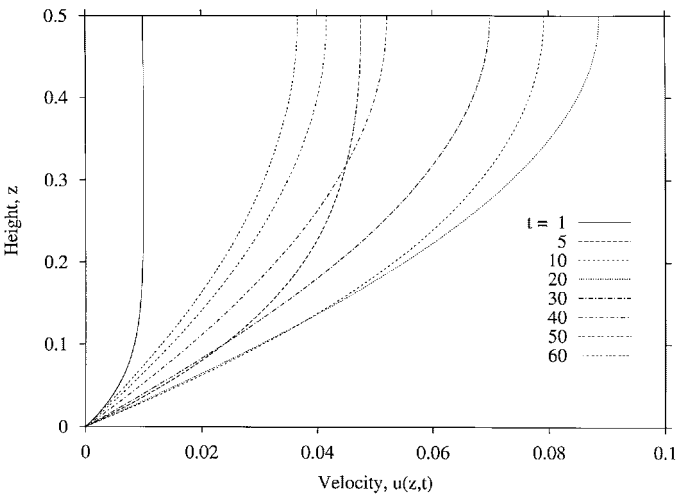

Figure 4. Velocity profiles, $u(z, t)$, across half the channel depth for a flow with $De = 10$, $Rv = 1$ and $\delta = 100$ for $t \in [1, 60]$.

of the flow field is inferred from Figure 4, where $u(z, t)$ is plotted against the height over the lower half of the channel, $z \in [0, 0.5]$, for different time stages, $t \in [1, 60]$. The parameter values in this case are $De = 10, Rv = 1$ and $\delta = 100$. The velocity exhibits a strong gradient near the wall initially, which weakens with time. In the channel core a plug-flow behaviour is

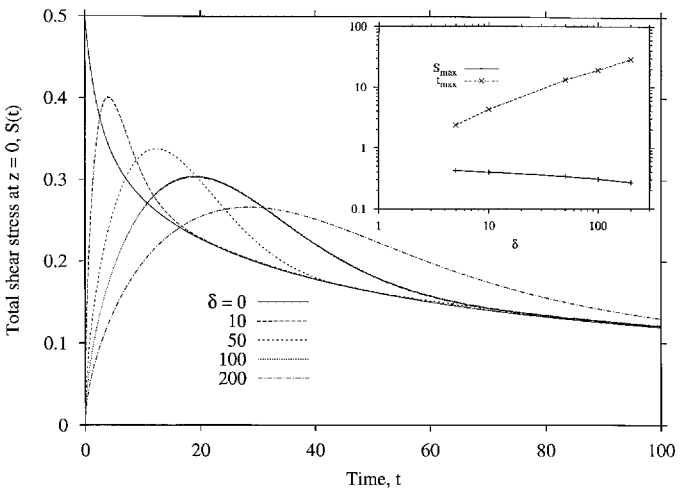

Figure 5. Influence of inertia on the evolution of the total shear stress, $S(t)$, at the wall ($z=0$), for a flow with $De=10$, $Rv=1$ and $\delta\in[0,200]$. Inset shows the dependence of the velocity maximum, $S_{\max}$, and correspondence time, $t_{\max}$, on δ.

observed in the early stages. The flat profile in the core region progressively disappears, and the flow becomes increasingly stronger near $z=0.5$, but only to weaken again as anticipated from Figure 2. The flow eventually becomes parabolic as predicted by expressions (33).

A similar response is observed for the total shear stress, $s(z,t)=aRvu_{x,z}(z,t)+\tau_{xz}(z,t)$. Figure 5 shows the evolution of the total shear stress at the wall, namely $S(t)=s(z=0,t)$. The stress exhibits initially a jump for $\delta=0$, which is independent of Rv and De, and is equal to $\frac{1}{2}$, as mentioned in Section 3.2. Similar to the velocity, the maximum shear stress, $S_{\max}$, decreases monotonically with δ. The inset indicates that $S_{\max}$ decreases with inertia at a smaller rate than the velocity, namely like $\delta^{-0.12}$, while the time at which the maximum occurs $t_{\max}/\delta$ behaves essentially similarly as before, like $\sqrt[3]{\delta}$. The profiles for $s(z,t)$ in Figure 6 correspond to those in Figure 4 ($De=10, Rv=1$ and $\delta=100$). Initially ($t<1$), the shear stress is essentially zero for $z>0.2$, reflecting the plug-flow behaviour inferred from Figure 4. As t increases ($t<10$), the overall stress increases in the channel core and near the wall. As t increases further, s behaves linearly with z, at which point the flow begins to behave like Poiseuille's.

The behaviour of the polymeric stress, $T(t)$, and normal stress, $N(t)$, at the wall departs somewhat from that of $U(t)$ and $S(t)$. Figures 7 and 8 depict the evolution of T and N against time. There is a strong buildup of stress upon flow inception, reaching a maximum, to then decrease asymptotically with time, as suggested by (35). Since the pressure (drop) is maintained constant, the normal force on the wall is directly dictated by normal stress. Thus, Figure 8 indicates that the normal force on the channel wall increases as the front moves, reaching a maximum that is not always increasing with inertia as one would anticipate. In fact, there is an optimum δ (in this case 50) for which the normal force is highest. Inertia appears to influence similarly both the normal and polymeric stresses. This is not the case regarding the influence of elasticity, which will be assessed next.

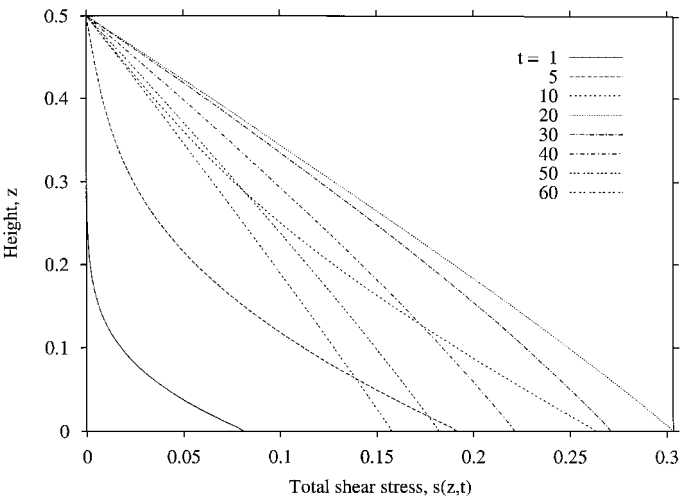

Figure 6. Total shear stress profiles, $s(z,t)$, across half the channel depth for a flow with $De = 10, Rv = 1$ and $\delta = 100$ for $t \in [1, 60]$.

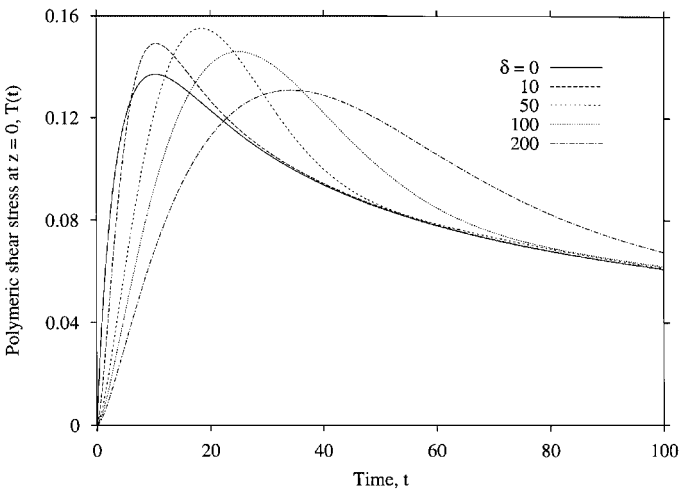

Figure 7. Influence of inertia on the evolution of the polymeric shear stress, $T(t)$, at the wall ($z = 0$), for a flow with $De = 10$, $Rv = 1$ and $\delta \in [0, 200]$.

4.2. *Influence of elasticity*

The influence of fluid elasticity is assessed by varying the relaxation time or De. Figure 9 depicts the evolution of the front position for the range $De \in [0, 100]$, $Rv = 1$ and $\delta = 100$. The front tends to accelerate significantly as the level of elasticity increases. The change in concavity indicates that the front eventually decelerates later for higher De, relaxing to Newtonian behaviour, as suggested by (35). Thus, similar to inertia (Figure 2), elasticity

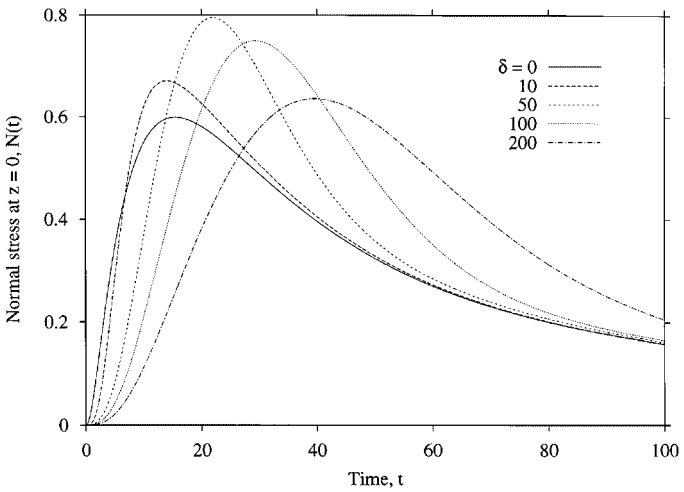

Figure 8. Influence of inertia on the evolution of the normal stress, $N(t)$, at the wall ($z = 0$), for a flow with $De = 10$, $Rv = 1$ and $\delta \in [0, 200]$.

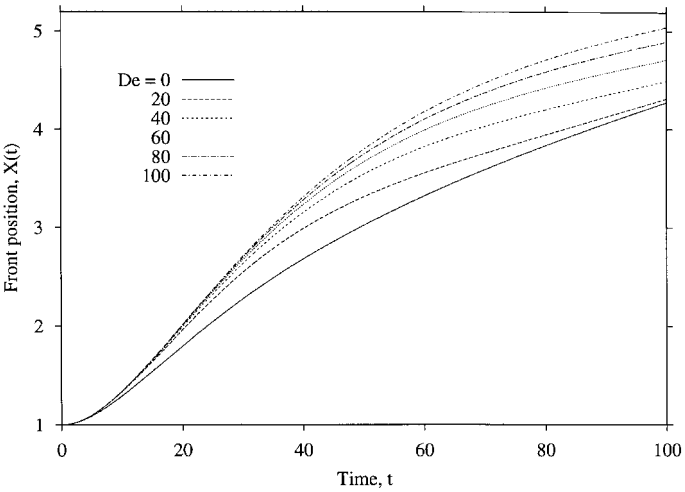

Figure 9. Influence of fluid elasticity on the evolution of the front position for a flow with $\delta = 100$, $Rv = 1$ and $De \in [0, 100]$.

tends to facilitate the fluid movement. The evolution of the front velocity (not shown) is also inferred from Figure 9, exhibiting a sharp rise similar to Figure 3. However, the thickness of the 'boundary layer', as well as the maximum velocity and the time at which it occurs are essentially unaffected by the level of elasticity. Similar remarks may be made concerning the total shear stress. However, the polymeric and normal stresses are worth examining closer.

The evolution of the polymeric shear stress and normal stress at the wall is shown in Figures 10 and 11, respectively. Note that both T and N vanish when $De = 0$. Although

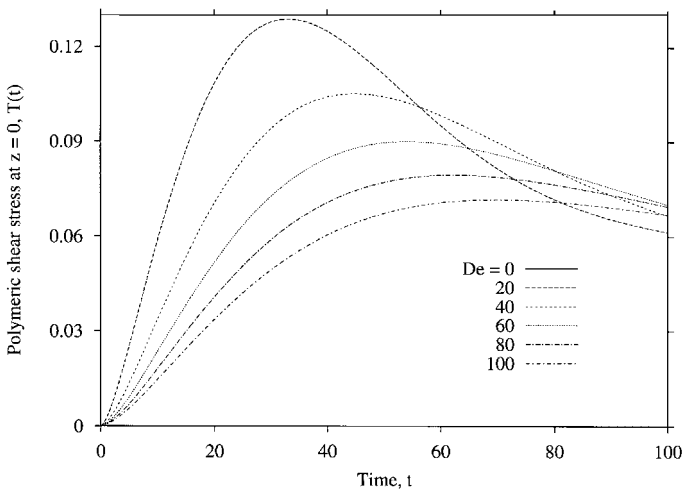

Figure 10. Influence of fluid elasticity on the evolution of the polymeric shear stress at the wall for a flow with $\delta = 100$, $Rv = 1$ and $De \in [0, 100]$.

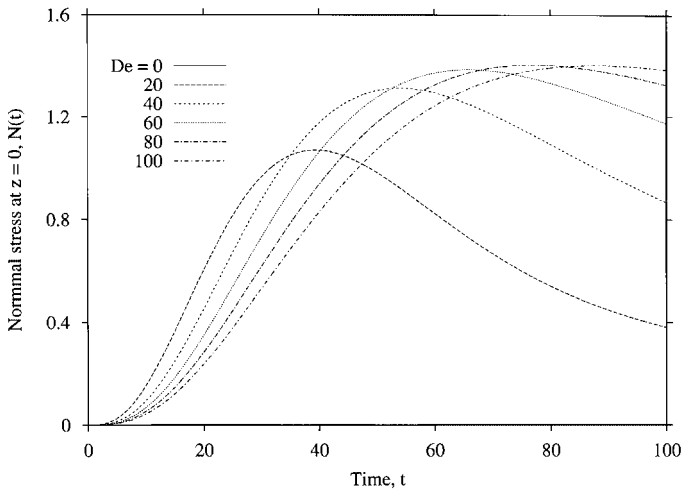

Figure 11. Influence of fluid elasticity on the evolution of the normal stress at the wall for a flow with $\delta = 100$, $Rv = 1$ and $De \in [0, 100]$.

elasticity is not expected to be influential at large t for T, as indicated by (35), it has a significant effect in the initial stages. As De increases, T decreases overall (from infinity in the limit $De \to 0^+$), but eventually tends to level off at large De. It is somewhat surprising that the level of the polymeric shear stress decreases as De increase. This, however, can be easily seen for the case of a purely elastic fluid ($\delta = 0$). In this case, expressions (28) lead to $T_{\max} = aP/12X$, which indicates that since X grows with time, so does the maximum polymeric shear stress. This behaviour is in sharp contrast with that of the normal stress,

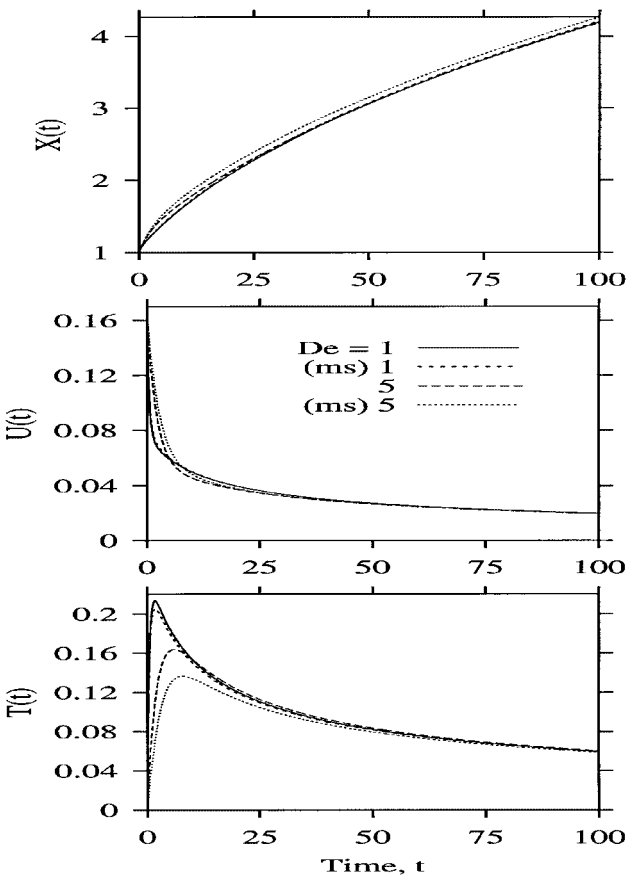

Figure 12. Flow behaviour at small Deborah number in the absence of inertia. Comparison between the multiple-scale and exact solution for X, U and T for $Rv = 1$ and $De = 1$ and 5.

which significantly increases with De. Typically, N exhibits a maximum earlier than T. The maximum is an indication of strong normal stress buildup in the moderately small De range ($De < 60$), but the stress tends towards a constant level for large De ($De > 60$).

The influence of elasticity is further examined in the limit of an inertialess fluid ($\delta = 0$). In this case, an analytical solution can be found by using the multiple-scale outlined above and in Appendix A. Solution (35) for the front position is practically insensitive to variation in De for small De, including the limit $De = 0$. This is expected since $X(t)$ does not exhibit a 'boundary layer' behaviour near $t = 0$ (see Figures 2 and 9). In contrast, the front velocity, $U(t)$, and especially the normal stresses vary sharply with t near inception (see Figure 4). The validity of the multiple-scale solution is assessed through comparison against the exact (numerical) solution. Comparison is carried out for small De (1 and 5), with $Rv = 1$. The results are shown in Figure 12 for the approximate and exact solutions for $X(t)$, $U(t)$ and $T(t)$. In general, comparison between approximate and exact (numerical) solutions indicates an excellent agreement in the lower range of De values. Even when $De > 1$, the figure shows

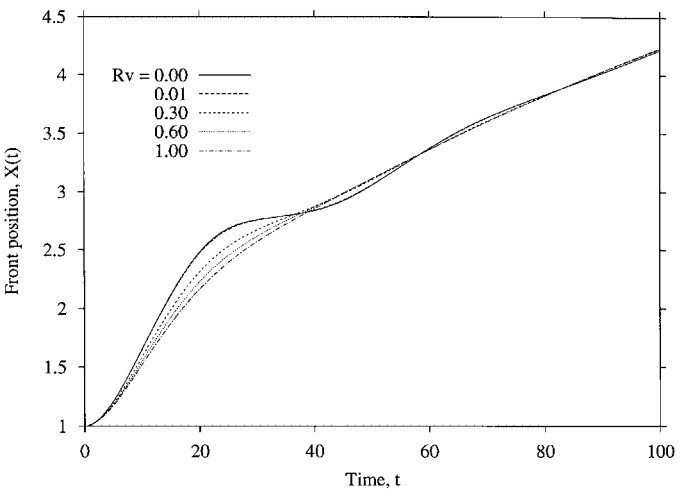

Figure 13. Influence of viscosity ratio on the evolution of the front position for a flow with $\delta = 50$, $De = 10$ and $Rv \in [0, 1]$.

good agreement for X and U, although for this range of De values, the approximate solution is not supposed to remain valid. The figure shows a significant discrepancy in the stress, especially for $De = 5$. The error is on the order of 5 and 20% for $De = 1$ and 5, respectively. The development of the boundary-layer region (near $t = 0$) is at the origin of the discrepancy.

4.3. *Influence of viscosity ratio*

The influence of elasticity is now assessed by varying the solvent-to-polymer viscosity ratio, Rv. In this section, the Deborah number is fixed at $De = 10$, and the Reynolds number at $\delta = 50$. The viscosity ratio varies over the range $Rv \in [0, 1]$, and includes Maxwell's fluid ($Rv = 0$). Although practical fluids may possess a relatively large viscosity ratio, it is generally found that no new dynamics emerges for $Rv > 1$, except that the rate of damping increases. Figure 13 displays the evolution of the front position, which reflects the onset of oscillatory motion as Rv is decreased towards zero. There is even a flattening of the X curve that typically happens close to inception, and which is most evident for a Maxwell fluid. At this point, the front essentially ceases to advance for some time until it is set in movement again (by elastic stress). The picture becomes clearer once the front velocity is inspected from Figure 14. The oscillatory response reflects a strong undershoot, with U reaching almost zero at the point where X is essentially flat. The oscillations decay with time, at a rate that increases with Rv. Figure 15 shows the velocity profiles for $Rv = 0.01$ and $t \in [1, 48]$, which illustrates clearly the sustenance of the plug-flow in the channel core over a long time ($t < 10$). The velocity gradient at the wall is essentially the same. For $t > 10$, the flow begins to behave like Poiseuille's, with decreasing velocity gradient and flow intensity. At about $t = 32$, the velocity exhibits a maximum at around 0.2. The bulge disappears later on, and the flow regains some strength, but never recovering its maximum level reached at $t = 10$.

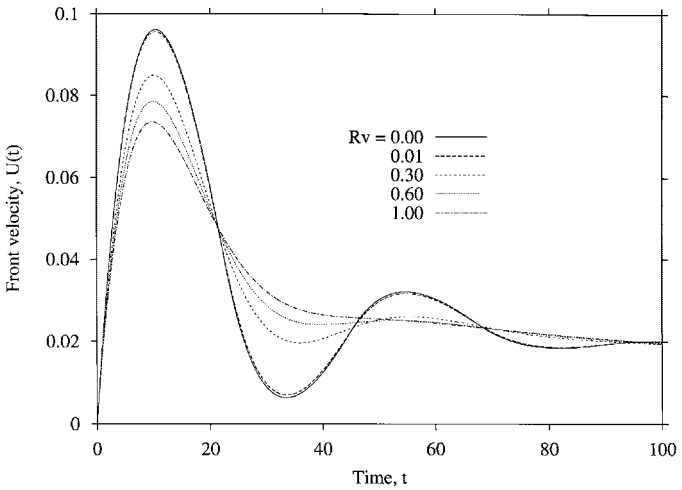

Figure 14. Influence of viscosity ratio on the evolution of the front velocity for a flow with $\delta = 50$, $De = 10$ and $Rv \in [0, 1]$.

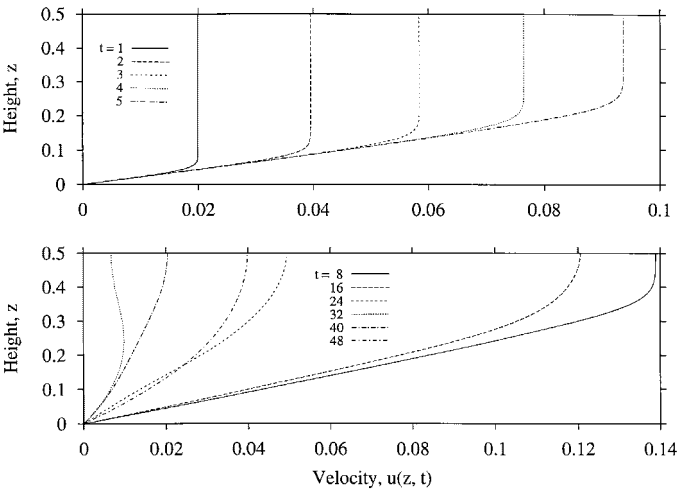

Figure 15. Velocity profiles, $u(z, t)$, across half the channel depth for a flow with $De = 10$, $\delta = 50$ and $Rv = 0.01$ for $t \in [1, 48]$.

The behaviour of the total and polymeric shear stresses, as well as that of the normal stress, is very similar, and is typically illustrated in Figure 16 (see also Figure 18), which depicts the influence of Rv on the evolution of T. The most striking feature in the figure is the emergence of singularities (discontinuities in $\dot{T}$) at the cusp(s) and trough(s) when $Rv = 0$. The occurrence of the singularities coincide with the change of concavity of U. Inspection of Equation (14) clearly indicates that, since the shear stress remains finite, the velocity gradient becomes itself singular. Indeed, additional results show that, when $Rv = 0$, the velocity $u(z, t)$

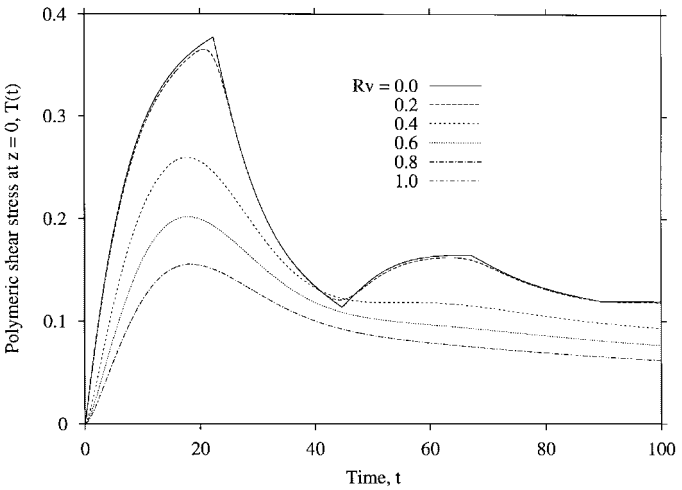

Figure 16. Influence of viscosity ratio on the evolution of the polymeric shear stress at the wall for a flow with $\delta = 50$, $De = 10$ and $Rv \in [0, 1]$.

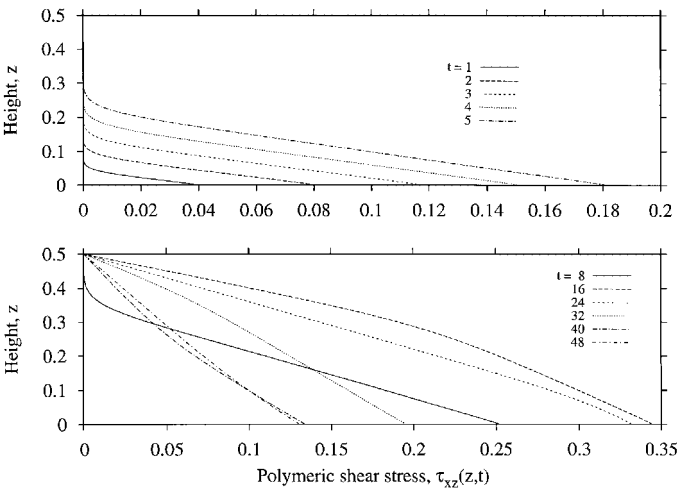

Figure 17. Polymeric shear stress profiles, $\tau_{xz}(z,t)$, across half the channel depth for a flow with $De = 10$, $\delta = 50$ and $Rv = 0.01$ for $t \in [1, 48]$.

becomes piecewise continuous, exhibiting a cusp at some z. The sharpness of the cusp is significantly reduced as Rv is slightly increased from $Rv = 0$, leading to the emergence of the maximum in $u(z,t)$, earlier depicted in Figure 15. The profiles for the polymeric stress $\tau_{xz}(z,t)$ are shown in Figure 17 at different times for $Rv = 0.01$, over the lower half of the channel. In the early stages, the stress typically remains zero over a significant portion of the channel, where the $u(z,t)$ is flat, to then increase essentially linearly with t everywhere in the channel. In particular, the stress $\tau_{xz}(z = 0, t)$ at the wall increases linearly with time, although the velocity gradient $u_{x,z}(z = 0, t)$ remains unchanged (see the top of Figure 15). Thus, most of the shear stress buildup at the wall originates from elastic effects. As t increases, the

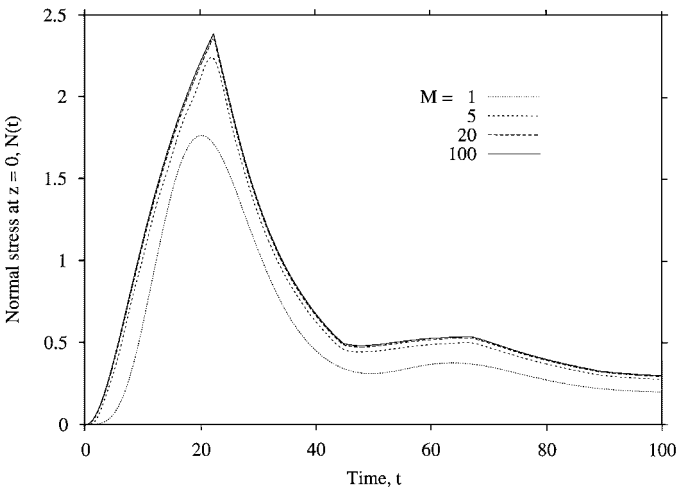

Figure 18. Influence of the number of modes on the evolution of the normal stress at the wall for a flow with $De = 10$, $\delta = 50$ and $Rv = 0$.

Table I. Influence of the number of modes on the value of X, U, S, N and T at $t = 100$, for a flow with $De = 10$, $\delta = 50$ and $Rv = 0$.

M	X	U	S	N	T
1	4.19127	0.01988	0.09748	0.19914	0.09748
5	4.21830	0.01998	0.11466	0.27574	0.11466
20	4.21859	0.01999	0.11825	0.29330	0.11825
100	4.21860	0.01999	0.11921	0.29810	0.11921

shear stress profile changes from positive to negative concavity at a time ($t = 16$) when the flow begins to lose intensity, to eventually exhibit a linear dependence on z, as Poiseuille conditions are recovered.

Finally, consider the influence of the number of modes on the convergence of the results. Figure 18 shows the evolution of the normal stress at the wall, $N(t)$, for $M \in [1, 100]$. In this case, $Rv = 0$, $De = 10$ and $\delta = 50$. This set of parameters have deliberately been selected to illustrate the influence of M given the transient dynamics involved. It is found that even with only one mode, the general qualitative picture is reasonably captured. Convergence is essentially attained for $M > 20$. The normal stress is usually most sensitive to the number of modes. The front position and velocity are the least affected by M. Table I displays the values for X, U, S, N and T at $t = 100$ for different M, which illustrates the lower rate of convergence for the stresses. In this study, all results reported are based on $M = 100$.

5. DISCUSSION AND CONCLUSION

In this study, the lubrication equations are derived for transient free-surface flow of Oldroyd-B fluids in narrow channels. The scaling of the polymeric shear and normal stresses is dictated by the upper-convective terms in the constitutive equations, and therefore may be different if

other constitutive models are used. The corresponding dynamic and kinematic conditions at the front are also derived for a thin film, leading to the vanishing of the pressure at the front (similarly to Newtonian fluids). The flow is assumed to be induced by a pressure gradient that is imposed at the channel entrance. In accord with the lubrication assumption, the pressure varies only in the streamwise direction, and, consequently, the front advancement can only be captured in the average sense in the depthwise direction, but the velocity and stresses can be obtained locally. The equations are then reduced for the case of developing free surface flow inside a straight channel.

For a straight channel, the problem reduces to two linear equations for the streamwise velocity component and polymeric shear stress, which are decoupled from the normal stress equations. However, the problem remains inherently non-linear because of the coupling of the flow field with front advancement (though the pressure gradient). The solution is sought in the form of Fourier representation for the velocity and stresses in the depthwise direction, which, upon Galerkin projecting onto the various modes, leads to a coupled system with $2M + 1$ degrees of freedom. The depthwise representation of the flow field of a thin film remains an open issue in the literature. A parabolic representation of the (streamwise) velocity component is usually adopted, even for transient and non-linear flows [10–12]. The film equations are obtained by integrating (averaging) over the channel depth. It is generally found that the depth-averaging procedure is valid for only a limited range of the Reynolds number. Additional calculations carried out but not reported in this study show indeed that the parabolic representation for the velocity, and linear representation for stress, leads to reasonable agreement with the Fourier solution over a wide range of the Reynolds and Deborah numbers for the front position and velocity, but remains a relatively poor approximation for the polymeric shear and normal stresses, especially in the initial stages of flow inception. A similar spectral representation has also been used previously for an open transient Newtonian film flowing on a substrate of arbitrary shape in the presence of inertia [13], leading to a much better agreement with Watson's similarity solution for steady film flow [17] than the depth-averaging solution [10].

Preliminary results are first obtained for some limit flows, namely the cases of a Newtonian fluid, flow with no inertia, and the general long-term behaviour for any fluid. The Newtonian fluid corresponds to a solution of infinite solvent viscosity ($Rv \to \infty$). In this case, the flow experiences an initial jump in velocity and stress that is proportional to the imposed pressure. The mean front position, $X(t)$, increases monotonically with time. For a purely elastic or inertialess fluid ($\delta = 0$), the problem is reduced to a second-order non-linear differential equation in X. A multiple-scale solution is obtained in the (singular) limit $De \to 0$. Comparison between the approximate and exact (numerical) solutions leads to excellent agreement when De is small (< 5). A sharp increase of the initial flow (velocity) is observed as the motion sets in, which is only exhibited by the multiple-scale solutions, and which cannot be recovered if a regular perturbation expansion is used in Re and De (see Figure 12). This is also the case in the Newtonian limit, which shows an initial jump in the flow. These observations are also confirmed from the numerical solution, which shows that the initial increase in flow is diminished by the effect of fluid elasticity. The long-term (asymptotic) solution shows that the flow behaviour is universal or independent of the flow parameters, as suggested by expressions (36) and (38).

The influence of inertia is examined by varying δ, keeping De and Rv fixed. Generally, the velocity and stresses exhibit an overshoot upon inception, to then decay asymptotically

with time like a Newtonian fluid. The maxima reached by the velocity and total shear stress (Figures 3 and 5) decreases monotonically like (inverse) power-laws in δ, which are practically uninfluenced by the values of De or Rv. The maxima reached by the polymeric and normal stresses increase with inertia in the small δ range ($\delta < 50$), but decrease with inertia for large δ (Figures 7 and 8). Upon inception, the velocity and stress profiles across the channel depth hint to a plug-flow behaviour in the channel core, and gradually tend toward Poiseuille flow with time (Figures 4 and 6). Regarding the influence of elasticity, the maximum in normal stress appears to grow monotonically with De, whereas that in the polymeric shear stress decreases with De (see Figures 10 and 11). The influence of elasticity is best illustrated by varying the viscosity ratio. It is found that for a small Rv value, the flow exhibits oscillatory response (see Figures 13 and 14), despite the static driving conditions. The plug-flow behaviour in the channel is clearly evident in this case (see Figure 15), and the velocity profile exhibits even a maximum close to the wall, which eventually disappears with time, when the flow recovers the parabolic profile.

The present study lays the mathematical foundation for the flow inside narrow channels of general shape. More importantly, the study elucidates clearly the conditions when complex dynamics can emerge, despite the simplicity in geometry and driving conditions. In particular, it is clearly shown that oscillatory behaviour for statically stressed flow, which result from fluid elasticity, arise only if both inertia and elasticity are significant.

APPENDIX A: MULTIPLE-SCALE SOLUTION

In order to use multiple-scale theory, Equation (29) must be rewritten in terms of the short scale, t'. This form allows the elimination of the secularity on the long scale:

$$12aRvX^2X'' + (12X^2 + De)X' - DeX = 0 \tag{A1}$$

where a prime denotes (total) differentiation with respect to t'. Formally, $X(t')$ in Equation (A1) has a perturbation expansion of the form:

$$X(t', t) = X_0(t', t) + DeX_1(t', t) + O(De^2), \quad De \to 0^+ \tag{A2}$$

Using the chain rule for the first and second derivatives, and collecting powers of De, give, to leading order, De^0:

$$X_{0,t't'} + \beta X_{0,t'} = 0 \tag{A3}$$

which admits the following solution:

$$X_0(t', t) = c_1(t) + c_2(t)\mathrm{e}^{-\beta t'} \tag{A4}$$

where $\beta = 1/aRv = Rv + 1/Rv$. To next order, De^1:

$$X_{1,t't'} + \beta X_{1,t'} = -2X_{0,tt'} - \beta X_{0,t} - \frac{\beta}{12X_0^2}(X_{0,t} - X_0) \tag{A5}$$

Substituting expression (A4) into the right-hand side of Equation (A5), and integrating once, leads to the following equation for X_1:

$$X_{1,t'} + \beta X_1 = \frac{\beta}{12}\left[\left(\frac{1}{c_1} - 12\dot{c}_1\right)t' + \frac{1}{\beta c_1}\ln(c_1 + c_2 e^{-\beta t'}) + \frac{1}{c_1 + c_2 e^{-\beta t'}} - \frac{12}{\beta}\dot{c}_2 e^{-\beta t'}\right] \quad \text{(A6)}$$

The particular solution for Equation (A6) indicates the presence of a secular term that grows like t', and another that behaves like $t' e^{-\beta t'}$. The first secular term is eliminated by setting

$$\dot{c}_1 - \frac{1}{12c_1} = 0 \quad \text{with solution } c_1(t) = \sqrt{\frac{t}{6} + d_1} \quad \text{(A7)}$$

where d_1 is a constant. It is not necessary to eliminate the second secular term since it decays exponentially with increasing t'. Recall that $t' = t/De$. Therefore, for all $t > 0$, it is valid to set $\dot{c}_2(t) = 0$ or $c_2(t) = d_2$, where d_2 is a constant. Upon imposing initial conditions $X(0) = 1$ and $\dot{X}(0) = 0$, the following expressions are obtained for the constants:

$$d_1 = \frac{1}{4}\left(1 \pm \sqrt{1 - \frac{De}{3\beta}}\right)^2, \quad d_2 = \frac{De}{12\beta\sqrt{d_1}} \quad \text{(A8)}$$

Although both branches give a real value for d_1, only the $(+)$ branch reduces to the Newtonian limit as $De \to 0$; it is thus this branch that will be kept. Finally, the solution to Equation (29) becomes, to leading order in De:

$$X(t) = \sqrt{\frac{t}{6} + d_1} + d_2 e^{-\beta t/De} + O(De), \quad De \to 0^+ \quad \text{(A9)}$$

where the expressions for d_1 and d_2 are given in (A8).

ACKNOWLEDGEMENTS

This work is supported by the Natural Sciences and Engineering Research Council of Canada.

REFERENCES

1. Floryan JM, Rasmussen H. Numerical methods for viscous flows with moving boundaries. *Applied Mechanics Review* 1989; **42**:323.
2. Khayat RE, Marek K. An adaptive boundary-element lagrangian approach to 3D transient free-surface flow of viscous fluids. *Engineering Analysis with Boundary Elements* 1999; **23**:111.
3. Hele-Shaw HS. The flow of water. *Nature* 1898; **58**:34.
4. Richardson S. Hele-Shaw flows with a free boundary produced by the injection of fluid into a narrow channel. *Journal of Fluid Mechanics* 1972; **56**:609.
5. Hieber CA, Shen SF. A finite-element/finite-difference simulation of the injection molding filling process. *Journal of Non-Newtonian Fluid Mechanics* 1980; **7**:1.
6. Zienkiewicz OC, Heinrich JC. A unified treatment of steady-state shallow water and two-dimensional Navier–Stokes equations—finite element penalty function approach. *Computer Methods in Applied Mechanics and Engineering* 1979; **17/18**:673.
7. Friedrichs B, Gueceri SI. A novel hybrid numerical technique to model 3-D fountain flow in injection molding processes. *Journal of Non-Newtonian Fluid Mechanics* 1993; **49**:141.
8. Chang RT, Powell TM, Dillon TM. Numerical models of wind driven circulation in lakes. *Applied Mathematical Modelling* 1976; **1**:141.
9. Weare RJ. Finite element or finite difference methods for the two-dimensional shallow water equations. *Computer Methods in Applied Mechanics and Engineering* 1976; **7**:351.

10. Chang HC. Wave evolution on a falling film. *Annual Review of Fluid Mechanics* 1994; **26**:103.
11. Hayashi H. Recent studies on fluid film lubrication with non-Newtonian lubricants. *JSME International Journal Series III* 1991; **34**:1.
12. Rushak KJ, Weinstein SJ. Viscous thin-film flow over a rounded crested weir. *Journal of Fluid Engineering* (*ASME*) 1999; **121**:673.
13. Khayat RE, Welke S. Influence of inertia, gravity and substrate topography on the two-dimensional transient coating flow of a thin Newtonian fluid film. *Physics of Fluids* 2001; **13**:355.
14. Bird RB, Armstrong RC, Hassager O. *Dynamics of Polymeric Liquids* (2nd edn), vol. 1. Wiley: New York, 1987.
15. Agassant JF, Avenas P, Sergent JPh, Carreau PJ. *Polymer Processing*: *Principles and Modeling*. Hanser Publishers: Munich, 1991.
16. Middleman S. *Fundamentals of Polymer Processing*. McGraw-Hill: New York, 1977.
17. Watson EJ. The radial spread of a liquid jet over a horizontal plane. *Journal of Fluid Mechanics* 1964; **20**:481.

